Remote Sensing of Environment 298 (2023) 113834

Contents lists available at ScienceDirect

Remote Sensing of Environment

journal homepage: www.elsevier.com/locate/rse

Evaluation of historic and new detection algorithms for different types of plastics over land and water from hyperspectral data and imagery

Alexandre Castagna [a,*,1], Heidi M. Dierssen [b,*,1], Lisa I. Devriese [c], Gert Everaert [c], Els Knaeps [d], Sindy Sterckx [d]

[a] Protistology and Aquatic Ecology, Ghent University, Krijgslaan 281, Ghent, 9000, East Flanders, Belgium
[b] Department of Marine Sciences and Geography, University of Connecticut, 1080 Shennecossett Road, Groton, 06340, CT, USA
[c] Flanders Marine Institute (VLIZ), InnovOcean Campus, Jacobsenstraat 1, Ostend 8400, West Flanders, Belgium
[d] Center for Remote Sensing and Earth Observation Processes, Flemish Institute for Technological Research (VITO), Boeretang 200, Mol, B-2400 Antwerp, Belgium

ARTICLE INFO

Edited by Jing M. Chen

Keywords:
Hydrocarbons/plastic detection algorithms
Plastics on land and water
Hyperspectral remote sensing
Airborne imaging

ABSTRACT

Several spectral indices have been proposed in the last decade for remote detection of macroplastics in the environment, however no comprehensive analysis has been provided on the sensitivity of those algorithms to different plastic types and their application to remote imagery over land and water. In addition, algorithm threshold values for plastic detection are typically variable per scene, and evaluation of how thresholds perform in multiple images is scarce. In this study we use a reflectance database of diverse pure plastic and non-plastic materials to evaluate spectral signatures for algorithm design and specificity evaluation, as well as to define optical classes for plastics. Published and new algorithms proposed in this study were then evaluated on three flight lines, comprising different observation geometries, of the Airborne Prism Experiment (APEX) sensor taken over Ostend, Belgium. Our results show that most common plastics cluster into two different categories based on their absorption features in the near infrared (NIR) and shortwave infrared (SWIR): Type 1 includes polyethylene, polypropylene, and vinyl, while Type 2 includes polyester, polystyrene, and acrylic. Nylon (polyamide) forms a separate spectral signature. Most line height algorithms were specific in the sense of mostly detecting plastic of either Type 1 or Type 2, while the evaluated ratio algorithms provided less distinction. All but one of the evaluated algorithms were found to have a threshold value that provided distinction between plastic and non-plastic materials (e.g., wood, concrete, algae, ice, etc.). Only the thresholds of the newly developed algorithms were consistent between the reflectance database and the imagery. Detection of macroplastic between flight lines was more consistent over land than over water. Floating transparent plastic bottles (Type 2) with plastic labels (Type 1) and floating polyethylene bags (Type 1) were only detected in one of the three flight lines. Our results support previous observations on the importance of high spatial resolution to minimize mixed spectral signals within a pixel, and points to the relevance of the thickness of the plastic layer influencing the detection for a given background and mixed signal. We also show that residual errors from atmospheric correction have a higher impact on the performance of ratio indexes than line heights. Our research suggests that the different plastic-specific algorithms can be used as complimentary metrics for plastic remote sensing, potentially enabling plastic optical type classification.

1. Introduction

Various algorithms and platforms have been proposed for optical remote sensing of plastics in the marine and terrestrial environments (Freitas et al., 2021; Lavender, 2022; Martínez-Vicente et al., 2019; Maximenko et al., 2019; van Sebille et al., 2020). Many of these algorithms detect bright spectral anomalies compared to background, but cannot discriminate plastic material from other types of objects that create those anomalies. Current literature often focuses on either controlled experiments or Sentinel-2 data with mixed spatial resolutions across wavebands that are subject to large uncertainties (Hu, 2021). And while several broadband ratios using shortwave infrared (SWIR)

* Corresponding authors.
E-mail addresses: alexandre.castagna@eoplus.scien (A. Castagna), heidi.dierssen@uconn.edu (H.M. Dierssen).
[1] These authors contributed equally.

https://doi.org/10.1016/j.rse.2023.113834
Received 18 August 2023; Received in revised form 20 September 2023; Accepted 23 September 2023

wavelengths have been successfully used to detect plastics on land (Asadzadeh and de Souza Filho, 2016; Zhang et al., 2022), these indices have not been applied to aquatic ecosystems which tend to have lower background SWIR reflectance and issues with sun glint.

From a hyperspectral perspective, several distinct spectral features were identified to be ubiquitous to naturally-harvested marine plastics, as well as from a collection of virgin plastic material (Garaba and Dierssen, 2018, 2020; Knaeps et al., 2021). Notably, four absorption features were identified at ≈931, 1215, 1417 and 1732 nm specific to hydrocarbons or plastics. The features at 931 and 1417 nm coincide with absorption bands of water vapour and would be challenging to measure from the top of the atmosphere. Several other studies have measured the spectral reflectance of naturally-harvested weathered plastic bottles and bags and determined that these diagnostic spectral features are not ubiquitous to all plastics. For example, the 1215 nm feature was not apparent in reflectance of both floating polyethylene terephthalate (PET) and expanded polystyrene (PS) plastics (cf. Table 1 for plastic names and acronyms). Also, a broader absorption feature centred at 1190 nm can be observed in polypropylene (PP) and PET. Additionally, the 1732 nm absorption feature was largely absent in observations of PET plastics, but an additional feature at 1660 nm was evident in prior works.

Spectral reflectance properties of plastics, including absorption band depth, width, and central waveband, also vary with plastic transparency, thickness, and shape. Spectral absorption features can be enhanced when targets have multiple layers separated by air, such as an intact plastic bottle (Goddijn-Murphy and Dufaur, 2018). Moreover, assessing the reflectance of semi-transparent material is challenging due to the contribution of reflectance from the background material, such as grass or sediment-laden water. Even controlled experiments can create artefacts when plastic material is placed over "black" materials or floating in containers that can reflect more light through the material than the natural environment creating larger absorption features and artificial water absorption features (Garaba et al., 2021a). This is especially problematic when evaluating floating plastics over clear water, which has a water-leaving reflectance lower than common "black" materials (Mobley, 1994).

This study evaluates published and new remote sensing algorithms for detecting different types of plastic material on land and floating on water. We evaluate the sensitivity and specificity of those algorithms on a large database of plastic and common non-plastic materials. And we evaluate the performance of those algorithms on airborne imagery from the Airborne Prism Experiment (APEX) sensor, including multi-meter scale artificial targets made of floating PET/PP bottles and LDPE bags.

2. Material and methods

2.1. Field campaign

The survey was conducted on 27 June 2019 on the eastern shore of the Spuikom, a lagoon in Ostend, Belgium (51°13′47.5" N 2°57′38.7″ E). Measurements were performed on floating targets placed on the lagoon and on structures in the shore, at the VZW Inside-Outside club. Details of targets, in situ measurements and airborne imagery are provided in the sections below.

Table 1
Acronyms of plastic types.

Acronym	Plastic name	Common name
ABS	Acrylonitrile butadiene styrene	–
EVA	Ethylene-vinyl acetate	–
PA	Polyamide	Nylon
PE (HDPE or LDPE)	Polyethylene (High- or low-density)	–
PET	Polyethylene terephthalate	Polyester
PMMA	Polymethyl methacrylate	Acrylic
PP	Polypropylene	–
PS	Polystyrene	–
PTFE	Polytetrafluoroethylene	Teflon
PVC	Polyvinyl chloride	Vinyl

2.1.1. Sampled targets

Selected targets on shore included asphalt, concrete walkway tiles (clinkers), small boats, PET bottles, and LDPE sheets from Flanders' standard waste bags for "Plastic or Metal packaging and Drink cartons" (PMD; Fig. 1). The floating PET bottles target was 3.0 m × 2.5 m. The floating PMD bags target was 4.0 m × 4.0 m and the PMD bags target over grass was 3.60 m × 3.20 m.

2.1.2. In situ reference measurements

Hyperspectral Lambert-equivalent bi-hemispherical reflectance, $\rho^{L}(\lambda)$, of anthropogenic targets were estimated using a portable spectroradiometer (ASD FieldSpec FR, Malvern Panalytical). The spectroradiometer measures radiance from 350 nm to 2500 nm at a nominal spectral sampling interval of 1.4 nm in visible to near-infrared (NIR) and 2 nm in the SWIR, with a nominal bandwidth of 3 nm in the visible-NIR and 10 nm in the SWIR. Measurements were conducted outdoors between 12:00 and 14:00 UTC under ambient light. Each measurement corresponds to the average of 30 sequential scans over a target sample spot, with ten different spots measured per sample. The instrument was fitted with an 8° field-of-view (FOV) lens, and operated in reflectance mode, using a 25 cm × 25 cm highly reflective (99%) diffuse reflectance panel (Spectralon, Labsphere) as a reference for determining the relative reflectance of the target. The hemispherical-directional measurements were converted to bi-hemispherical by scaling the measured values by π sr, the conversion factor if the targets had an isotropic reflectance distribution.

The interdetector steps in the spectral data resulting from the overlapping of main detectors VNIR, SWIR1 and SWIR2 were adjusted by applying a splice correction. A splice correction is not based on any physical model (Hueni and Bialek, 2017), but mitigates artefacts in the spectral shape and magnitude. Missing data is related to the spectral regions affected by strong light absorption by atmospheric gases, around ≈1400 nm and ≈1800 nm. Data is available in open access on PANGAEA (Garaba et al., 2021b).

Background diffuse water reflectance, $\rho_{w}^{*,L}(\lambda)$, was estimated using another spectroradiometer (FieldSpec HandHeld, Analytical Spectral Devices). The instrument measures radiance from 325 nm to 1075 nm at a nominal spectral sampling of 1.4 nm and a bandwidth of 3 nm. The skylight-blocked approach (Lee et al., 2019; Tanaka et al., 2006) was utilized to avoid specular reflectance. A grey diffuse reflectance panel (Spectralon, Labsphere) with nominal 12% reflectivity (Castagna et al., 2019, 2022) was used as reflectance reference. In total, measurements were performed in eight stations in the lagoon. Due to the negligible water-leaving signal in the SWIR as a result of the high absorption coefficient of pure water, the visible-NIR measurements were extrapolated to the SWIR range by using the last NIR band as a constant. Data from eight water stations were combined to provide an average $\rho_{w}^{*,L}(\lambda)$ of the lagoon for the period of the overflights.

The spectral reflectance of the targets is presented in section S1 of the supplementary material.

2.1.3. Airborne imagery

Imagery over the Spuikom and its surroundings were acquired with the APEX sensor mounted on a Cessna 208B Grand Caravan EX aircraft. The instrument is operated by the Flemish Institute for Technological Research (VITO). The sensor records upwelling radiance from 375 nm to 2498 nm, discretized in 299 bands, with a spectral sampling distance ranging between 2.5 nm to 14 nm and bandwidth ranging from 3 nm to 20 nm measured as the full width at half maximum. Considering the aircraft altitude and the sensor FOV, data were collected at a nominal 1.6 m × 1.6 m spatial resolution. Three flight lines (named a01c, a02c,

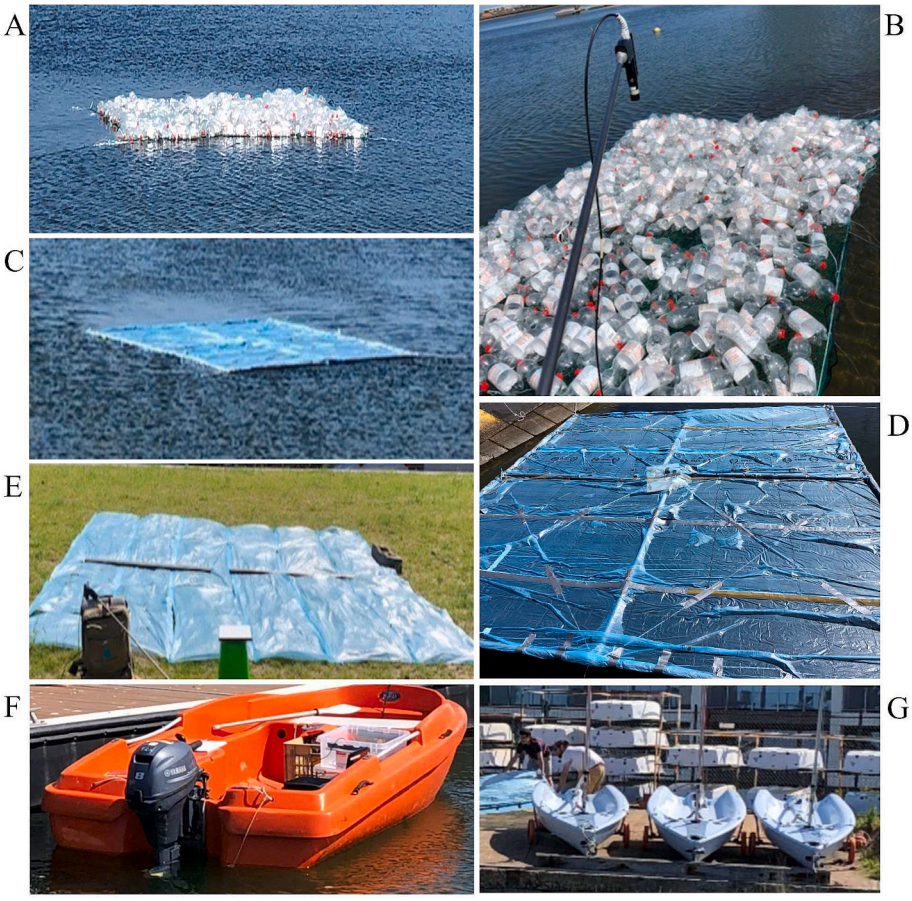

Fig. 1. Plastic reference targets used in the 27 June 2019 experiment on the Spuikom reservoir included: (A and B) collection of empty floating PET bottles with reflectance measured from the dock and then moved away; (C and D) floating PMD bags (LDPE) attached to a PVC frame; (E) dry PMD bags (LDPE) placed on grass. Additional plastic material sampled include (F) floating orange plastic boats, and (G) white and blue sailboats on land. (For interpretation of the references to colour in this figure legend, the reader is referred to the web version of this article.)

a06c) with different azimuthal orientations were performed over the region of interest. Imagery acquisition was completed in ≈39 min: a01c (10:01 to 10:04 UTC), a02c (10:09 to 10:11 UTC), and a06c (10:36 to 10:40 UTC). The step-by-step procedure performed to generate surface reflectance data used in this study is summarized in Fig. 2.

Radiometric calibration was performed by VITO to convert raw sensor data into at-sensor radiance (Schaepman et al., 2015; Taubert et al., 2013). A "smile correction" was applied to provide spectral co-registration over the detector surface, using splines to interpolate the radiometric measurements to a common spectral grid. The targets were

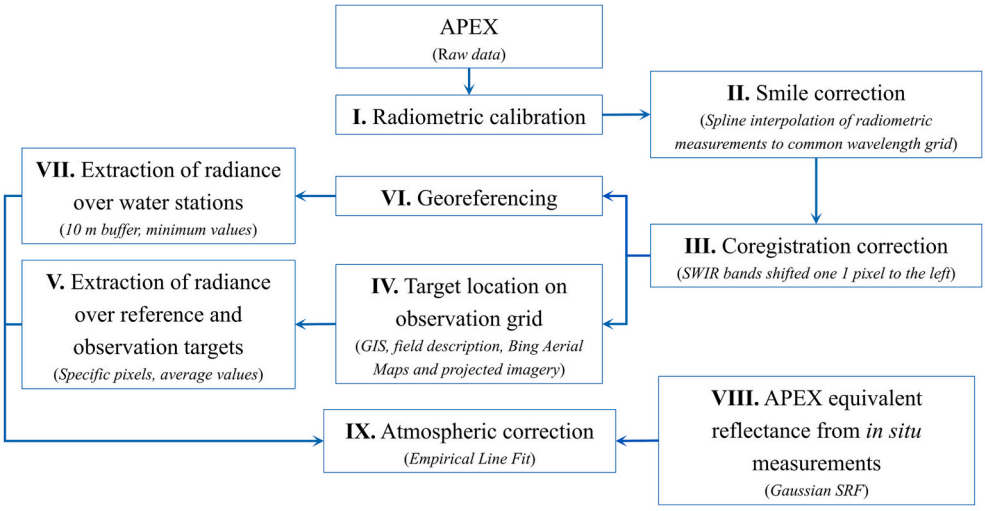

Fig. 2. A schematic of the processing steps for the hyperspectral Airborne Prism Experiment (APEX) imagery acquired over the Spuikom, Ostend, Belgium on 27 June 2019.

analysed in the observation geometry to avoid introducing artefacts from the spatial interpolation to a projected grid. A left-shift of 1 pixel was necessary for the wavebands 109 to 299 (958 nm to 2498 nm) to provide spatial co-registration with the visible-NIR bands. Reference targets over land and plastic targets floating on the water were visually located on the observation grid of each image using Global Positioning System (GPS) coordinates, true colour composites, aerial maps from Bing, and projected versions of the imagery produced specifically for this purpose (Fig. 3). Water calibration points were extracted from the projected imagery using a 10 m radius buffer and selecting the minimum radiance at each band to reduce the impact of the sky and sun glint.

The empirical line method (ELM; Smith and Milton, 1999) was applied to compensate for optical effects of the atmosphere layer between the sun-surface and surface-sensor. Here, ELM was based on regression analyses of in situ $\rho^{L}(\lambda)$ against airborne at-sensor radiance over the same reference targets. The reference targets are required to be (i) spatially homogeneous in a spatial scale larger than that of the sensor instantaneous FOV to avoid mixed spectral signals and (ii) to cover, in all spectral bands, the possible range of reflectance of the observation targets, such as to not require extrapolation of the regression relation. Three reference targets on land that satisfied these requirements in the visible and near-infrared were: the asphalt, the grey clinkers, and pink clinkers. Since the grey and pink clinkers only present spectral differences in the visible range, the PMD bags (LDPE) on grass was used as an additional calibration point for the ELM. All land targets were brighter in the SWIR than the floating plastic targets, so $\rho_{w}^{*,L}(\lambda)$ was included as a lower calibration point. Prior to the regressions, the in situ measurements were converted into APEX-equivalent wavebands by averaging the in situ spectra with Gaussian relative spectral response functions (SRF) with matching sensor waveband centres and widths (Jehle et al., 2015). An example of the ELM procedure is provided in section S1 of the supplementary material.

APEX wavebands were also aggregated as necessary to provide the same wavelength coverage as the wavebands of the sensors for which the tested published algorithms were originally developed for. The details of the band aggregation are provided in Section S2 of the supplementary material.

Imagery visualization and analyses were performed in R version 3.6.3 (Team, 2020) with aid of packages “raster” version 3.4–13 (Hijmans, 2021) and “rgdal” version 1.5–23 (Bivand et al., 2021). Several visualizations of spectral quantities in this study were normalized by the spectral integral of that quantity in the same spectral range as presented in the visualization. Those quantities are here called ‘integro-normalized’.

2.2. Compiled dataset of plastics and other materials

A dataset of previously published reflectance measurements was compiled with an assortment of plastics including: ABS ($n = 2$), PA (n = 2), PE ($n = 23$), PET ($n = 6$), PMMA ($n = 1$), PP (n = 1), PS (n = 1), PTFE (n = 1), PVC (n = 6) and mixed unknown plastics ($n = 7$; Garaba and Dierssen, 2017). The dataset was augmented with common construction materials (e.g., concrete, wood, brick, fabric, metal, fiberglass; Kokaly et al., 2017; Knaeps et al., 2020) and other potential bright floating targets (e.g., macroalgae, whitecaps, ice; Dierssen, 2019; Khan et al., 2017; Hu et al., 2017; Qi et al., 2021; Wang et al., 2018). The reflectance measurements of brine shrimp (Artemia) cysts by Qi et al. (2021), Ulva by Hu et al. (2017), and Sargassum by Wang et al. (2018) were used at the highest biomass concentration. The non-plastic targets added to the dataset could potentially be observed on imagery over land and water, and will help to evaluate if the algorithms are effective in discriminating plastic from other materials.

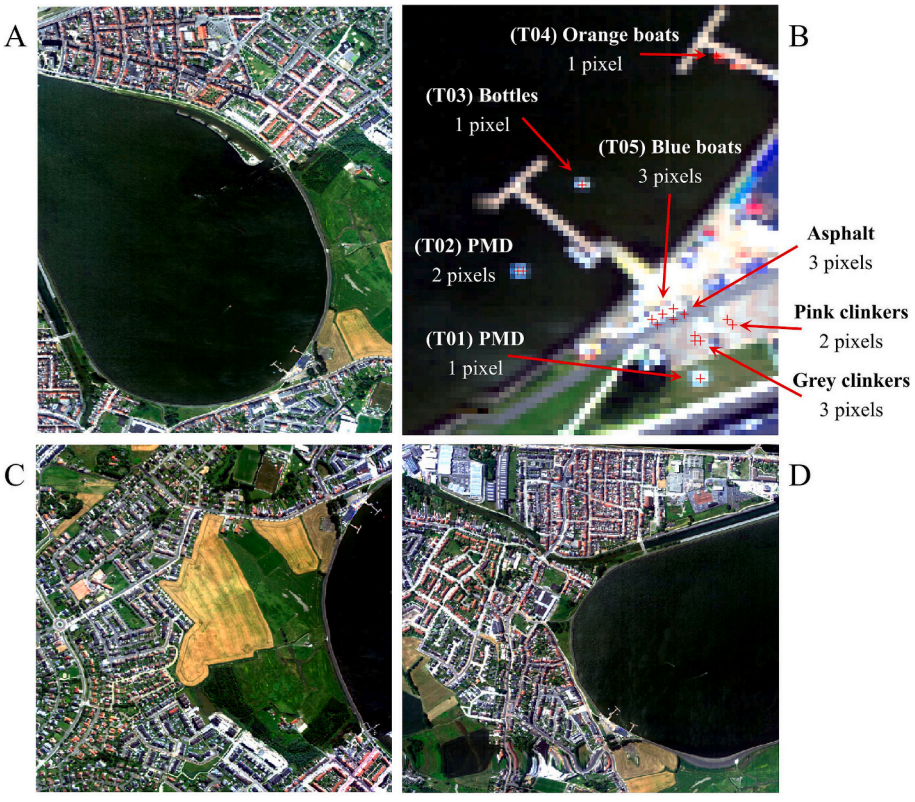

Fig. 3. Pseudo true-colour APEX imagery in the observation grid, acquired on 27 June 2019 over the Spuikom, Belgium. (A) flight line a02c; (B) flight line a02c showing ground reference pixels representing the targets; (C) flight line a01c; and (D) flight line a06c. Plastic targets include: T01 - PMD on grass; T02 - PMD on water; T03 – PET bottles on water; T04 - Orange boats; T05 – Blue and white boats. (For interpretation of the references to colour in this figure legend, the reader is referred to the web version of this article.)

The subset of the dataset containing only plastics was subject of a cluster analysis with the K-means algorithm (Forgy, 1965). The K-means algorithm looks for an optimal arrangement of samples into a user-defined number of groups in order to minimize within-group variance. Prior to the analysis, the spectral range of strong atmospheric absorption was excluded and the data was integro-normalized in the range of 1000 nm to 1800 nm. The spectra with nearly flat spectral shapes were manually separated into a cluster of "featureless spectra" in the wavelength range of interest before the K-means application. The objective of the analysis was to observe common patterns in spectral features and support algorithm development in this spectral range.

2.3. Plastic detection algorithms

A set of algorithms for plastic detection were evaluated with the compiled dataset and with the airborne imagery (Table 2). The tested algorithms are divided into two classes: line-height indexes and ratio indexes. Line heights algorithms typically concern three wavebands, where the signal is taken as the difference of the value of the middle band to the linear interpolation of the values of the other bands. Ratio algorithms involve the ratio of reflectance values, directly on wavebands or after addition or subtraction operations between a set of wavebands.

The previously published line height indexes tested here were the so called "hydrocarbon indexes" (HI) centred at 1215 nm (Garaba and Dierssen, 2018), and at 1732 nm (Kühn et al., 2004). The previously published ratio indexes tested here were the Advanced Plastic Greenhouse Index (APGI; Zhang et al., 2022), the normalized difference plastic index (NDPI; Guo and Li, 2020), and the relative-absorption band depth (RBD; Asadzadeh and de Souza Filho, 2016). We also evaluated a new line height and a new ratio index developed in this study: the line height index centred at 1675 nm (HI_1675), and a normalized difference index using two aggregated SWIR wavebands centred at 1610 and 1715 nm (ND_1715; Table 2). The choice of bands for these algorithms was based in the spectral analysis of plastic and non-plastic targets presented in section 3.1 and details are further discussed in section 4.2.

Sources: HI_1215 (Garaba and Dierssen, 2018); HI_1675 (this study); HI_1732 (Kühn et al., 2004); APGI (Zhang et al., 2022); NDPI (Guo and Li, 2020); ND_1715 (this study); RBD (Asadzadeh and de Souza Filho, 2016).

Thresholds were determined visually for each index to identify the maximum number of known targets while preventing false positives. Thresholds were first determined on the compiled reflectance database of plastics and other materials to identify the limits where different sets of plastics could be distinguished. The thresholds were then adapted when necessary for application to the imagery. A single threshold was applied to the three flight lines to evaluate effects of artefacts in mixed pixels and atmospheric correction. Additional information on the imagery thresholds, including index values and contours are provided in Section S3 of the supplementary material.

All ratio algorithms (NDPI, ND_1715, and RBD) showed sensitivity to atmospheric correction issues over dark water surfaces that included some negative reflectance values in the SWIR bands (see Section S4 of the Supplemental material). Those errors related to atmospheric correction are discussed in section 4.3. To avoid retrieval of noise over water due to low signals in the SWIR, a mask was applied to remove pixels where the average reflectance between 920 and 1090 nm was < 0.01.

3. Results

3.1. NIR/SWIR characterization of selected plastics and non-plastic materials

With a few exceptions, non-plastic construction materials have flatter spectral shapes with no significant absorption bands between 1000 nm and 1800 nm (Fig. 4A). Brine shrimp cysts had a spectral shape similar to wood, with relatively subtle spectral features, but mostly a positive spectral slope in the two SWIR regions, separated by an offset (Fig. 4B). The photosynthetic organisms included in the dataset had a spectral shape similar to whitecaps, which can be expected considering their high water composition. Overall, the spectral features of non-plastic targets are quite different from the spectral shapes of fiberglass and plastics (Fig. 4C and D). Fiberglass is a glass fiber-reinforced plastic, and the spectral features of the plastic material are dominant in the reflectance spectra. Most of the plastic material exhibited a striking decreasing slope in the SWIR reflectance around 1600 nm that was unique compared to the non-plastic targets, which is the basis of the new broadband SWIR algorithm (ND_1715; Table 2).

Since plastic materials showed a diversity of spectral shapes across the NIR and SWIR, a cluster analysis was performed to find a reduced number of optical classes that could potentially be identified from NIR-SWIR measurements (Fig. 5). The cluster analysis identified six broad clusters of plastic reflectance spectra across the NIR and SWIR wavelengths. The first cluster represented plastics with nearly featureless reflectance (Fig. 5A) indicative of low concentration or thickness of material. The second and third clusters were comprised mainly of PVC and PE plastics, with absorption features centred around 1215 nm and 1720 nm (Fig. 5B and C). The only sample of PP material was grouped in Cluster 3 together with PE and PVC. Features in Cluster 3 were more pronounced than those in Cluster 2, which could be a result of a stronger absorption magnitude (higher concentration of the absorptive material). This could also help explain the dampened features in Cluster 1, mostly composed of the same PE plastics that were observed in Clusters 2 and 3. Clusters 4 and 5 were composed mostly of PET, PMMA, and PS, with

Table 2
Detection indexes tested on the APEX hyperspectral image obtained on 27 June 2019 over the Spuikom, Belgium. The APEX bands were aggregated to cover the same spectral ranges as those proposed in the published algorithms. The spatial resolution for airborne sensors are the ranges of typical operating heights, while for spaceborne sensors is the lowest spatial resolution of the used wavebands.

Index	Algorithm	Sensor	Resolution
HI_1215	$(1223-1203)\frac{\rho^{L}(1243)-\rho^{L}(1203)}{1243-1203}+\rho^{L}(1203)-\rho^{L}(1223)$	AVIRIS	2–20 m
HI_1675	$(1675-1604)\frac{\rho^{L}(1753)-\rho^{L}(1604)}{1753-1604}+\rho^{L}(1604)-\rho^{L}(1675)$	APEX	2–5 m
HI_1732	$(1728-1702)\frac{\rho^{L}(1745)-\rho^{L}(1702)}{1745-1702}+\rho^{L}(1702)-\rho^{L}(1728)$	HyMap	2–10 m
APGI	$100\rho^{L}(439)\rho^{L}(664)\frac{2\rho^{L}(831)-\rho^{L}(664)-\rho^{L}(2203)}{2\rho^{L}(831)+\rho^{L}(664)+\rho^{L}(2203)}$	MSI/Sentinel-2	20 m
NDPI	$\frac{\{\rho^{L}(1571)-\rho^{L}(1732)\}+\{\rho^{L}(2165)-\rho^{L}(2329)\}}{\rho^{L}(1571)+\rho^{L}(1732)+\rho^{L}(2165)+\rho^{L}(2329)}$	WorldView-3	4 m
ND_1715	$\frac{\overline{\rho}^{L}(1590\text{to}1630)-\overline{\rho}^{L}(1695\text{to}1735)}{\overline{\rho}^{L}(1590\text{to}1630)+\overline{\rho}^{L}(1695\text{to}1735)}$	APEX	2–5 m
RBD	$\frac{\rho^{L}(1660)+\rho^{L}(2165)}{\rho^{L}(1732)}$	WorldView-3	4 m

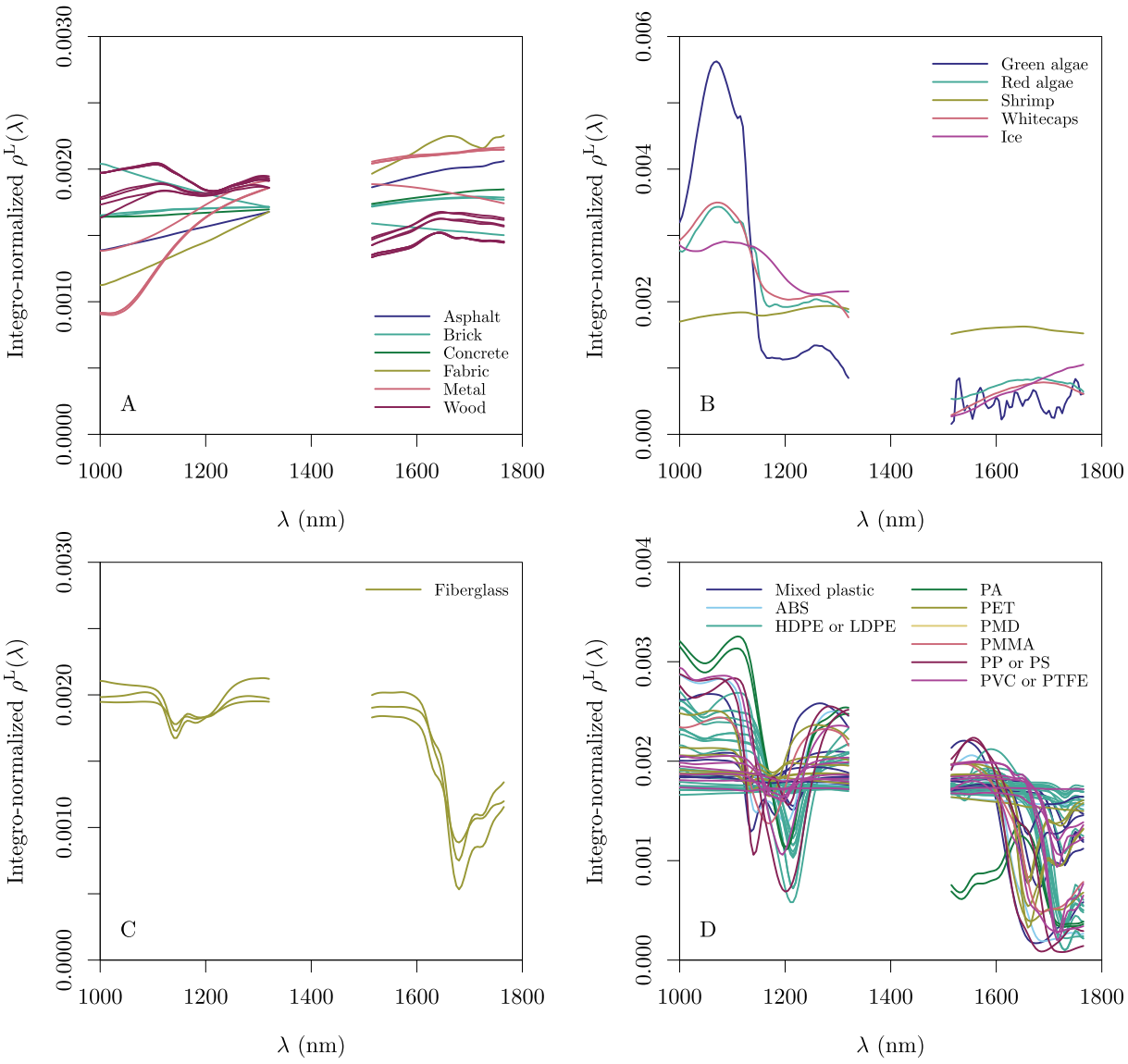

Fig. 4. Lambert-equivalent reflectance spectra normalized to the integral from 1000 to 1800 nm for (A) non-plastic construction material; (B) assortment of floating matter including algae, whitecaps, and ice; (C) fiberglass; and (D) plastics.

blue-shifted absorption features centred near 1135 nm and 1660 nm (Fig. 5D and E). The proposed HI_1675 algorithm was designed to capture this spectral signature. Cluster 4 had a sharper rise in reflectance in the SWIR bands (1660 to 1800 nm) compared to Cluster 5, and a subtler absorption feature at ≈1720 nm. The spectral shapes suggest that as with Clusters 2 and 3, Clusters 4 and 5 represent the same absorption bands, but at different magnitudes. The higher magnitude of the absorption bands would better define the absorption features around 1150 nm in reflectance space, but it would result in loss of detail around 1700 nm due to the lower reflectance boundary at 0. Cluster 6, comprised of PA, had absorption bands similar to Clusters 2 and 3, but with an additional absorption feature in the SWIR from 1535 to 1605 nm (Fig. 5F).

Broadly, we define three different groupings of plastic materials based on the NIR/SWIR absorption features (Table 3). Type 1 has absorption bands around ≈1215 nm and ≈1730 nm that represents the PP and PE plastics that typically comprise floating microplastics. Type 2 has bands that are blue-shifted centred at ≈1135 nm and ≈1660 nm. The composite material Fiberglass is included in Type 2, though the absorption feature at ≈1660 nm is red-shifted to 1684 nm. Nylon (PA) was considered Type 3 with similar bands to Type 1, but with strong absorption features around ≈1535 to 1605 nm.

The above analysis suggests that, depending on the specific design of anchor or normalization wavebands, algorithms extracting information around 1215 nm and 1730 nm are expected to detect Types 1 and 3, while algorithms extracting information around ≈1135 nm, ≈1670 nm would detect Type 2. Algorithms with additional absorption bands at 1535 and/or 1605 nm could identify nylon (PA) from other Type 1 plastics.

3.2. *Evaluation of specificity plastic detection algorithms*

The indices from Table 2 were applied to the compiled database of plastic and other materials (Fig. 6). With one exception, all algorithms were capable of differentiating plastic materials from non-plastic materials (Fig. 6). The exception was the APGI algorithm, which showed a large overlap of the index value between plastic and non-plastic materials (Fig. 7). Application of APGI may be constrained to datasets without significant presence of wood and ice (cf. section 4.2).

The HI_1215 and HI_1732 indexes were generally able to distinguish Type 1 plastics with better performance of the HI_1732 index which was also capable of differentiating some plastics in Clusters 1 and 4 (Fig. 6A

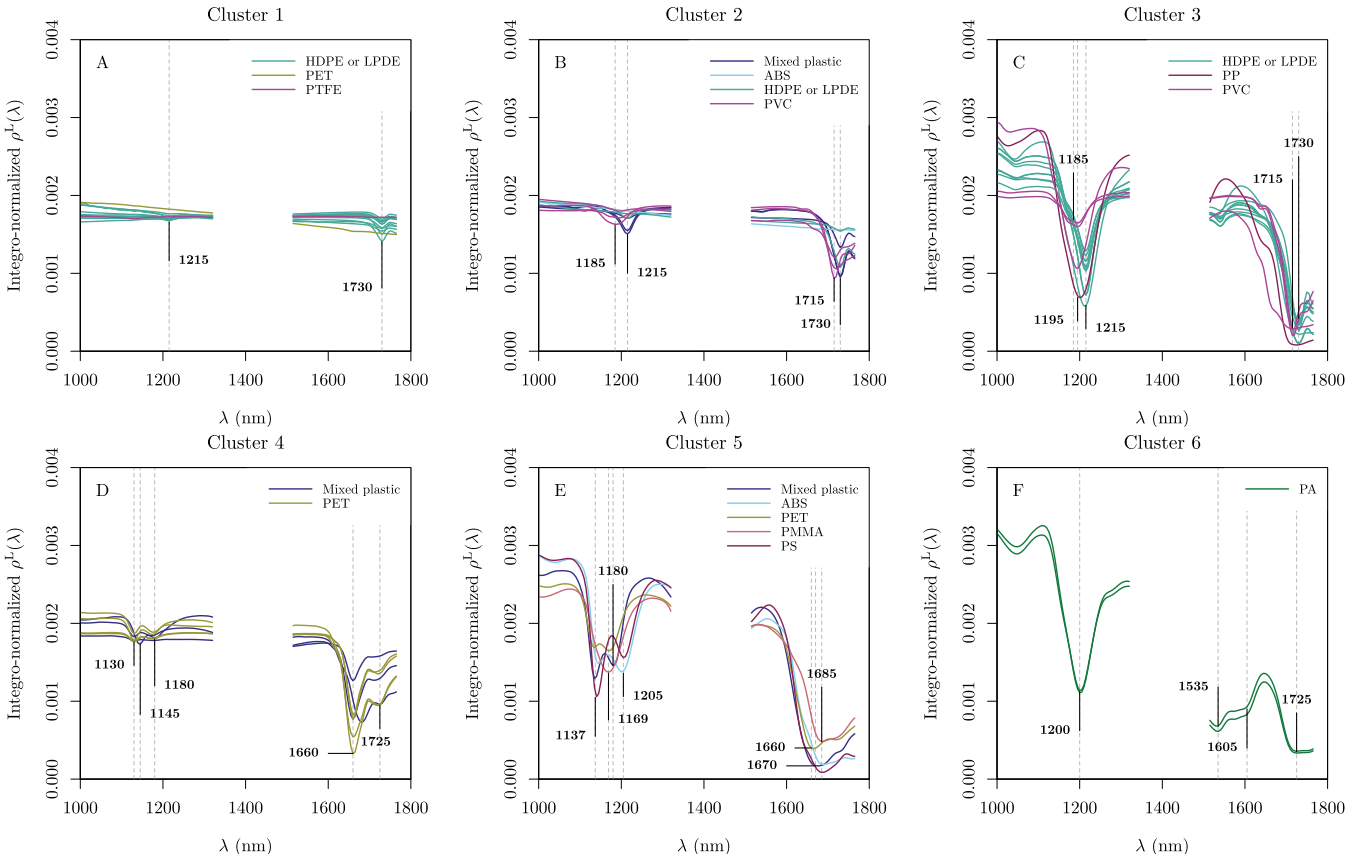

Fig. 5. Cluster analysis of plastic reflectance from the compiled database over the spectral range from 1000 to 1800 nm. The spectral gap centered at 1400 nm corresponds to the spectral region where the atmosphere is opaque and the signal is low. Dotted lines highlight minima related to absorption features. Type 1 is Cluster 2, 3 and 6; Type 2 is Cluster 4, 5; Type 3 is Cluster 6 with extra absorption bands at 1535 and 1605 nm.

Table 3
Broad grouping of plastic types based on identifying NIR/SWIR spectral absorption bands. Absorption features are generally centered within ±10 nm from values reported here for different plastics.

Type 1[†]	Type 2[††]	Type 3[†††]
(1215, 1730 nm)	*(1135, 1670 nm)*	*(1535, 1605 nm)*
PE (HDPE or LDPE)	PET	PA
PP	PMMA	
PVC	PS	
PA	ABS	
	Fiberglass	

[†] Type 1 includes plastics in Clusters 2, 3 and 6.
[††] Type 2 includes plastics in Clusters 4 and 5.
[†††] Type 3 includes plastics in Clusters 6.

and C). The HI_1675 index provided a strong differentiation between plastics of Type 2 from other materials, with the exception of two PVC samples of Cluster 3 (Fig. 6B). This index was designed as a compromise to capture plastics and fiberglass in Type 2, with the main absorption feature at 1660 nm or 1684 nm.

The NDPI and the ND_1715 captured a similar pattern across samples (Fig. 6D and E) as they target the same feature around ≈1720 nm. These ratio algorithms result in more generic discrimination of plastics from non-plastic materials and show little potential for plastic group discrimination. Like the NDPI, the RDB was designed for WorldView-3 wavebands and extracts a relative signal of the absorption feature at ≈1720 nm. However, its lower wavelength anchor point is located at ≈1660 nm, mostly preventing the discrimination of plastic materials of Type 2 (Fig. 6F). We note that the ND_1715 algorithm can also be applied to WorldView-3, using bands SWIR-3 and SWIR-4.

All the line height indexes showed the potential for positive and negative thresholds with the compiled dataset, while ratio algorithms allowed for a single, positive, threshold. The threshold values are presented in Table 4.

3.3. Water and floating targets viewed in APEX imagery

Comparison of atmospherically-corrected APEX spectra from the three flight lines with the field measurements of floating plastics revealed similar spectral shapes, with some differences in magnitudes (Fig. 8). The reference and retrieved spectra were very similar for the wet PMD bags (LDPE). The difference was higher for the plastic bottles and the orange boats. This is likely the effect of mixed pixels due to the target size and layout of the observation grid. The PMD bags were the largest target, forming a square target of 16 m^2. The PET target was a smaller rectangular target of 3 m × 2.5 m. The orange boats were even smaller targets, with dimensions of ≈2.5 m × 1.5 m.

The average water reflectance (Fig. 8D) has an order of magnitude lower reflectance compared to the plastic targets. Hence, water was used as a dark calibration point for the ELM-atmospheric correction. While there are apparent differences between the field and APEX reflectance, the amount is very small compared to the other targets (≈0.01 in the SWIR). As noted in the methods, pixels with reflectance at 1000 nm less than 0.01 were masked out to avoid noise in the plastic retrievals over water using SWIR band ratios.

3.4. Application of plastic detection algorithms to APEX imagery

The detection indexes presented in Table 2 applied to each APEX imagery over the Spuikom and surroundings are shown in Fig. 9, Fig. 10,

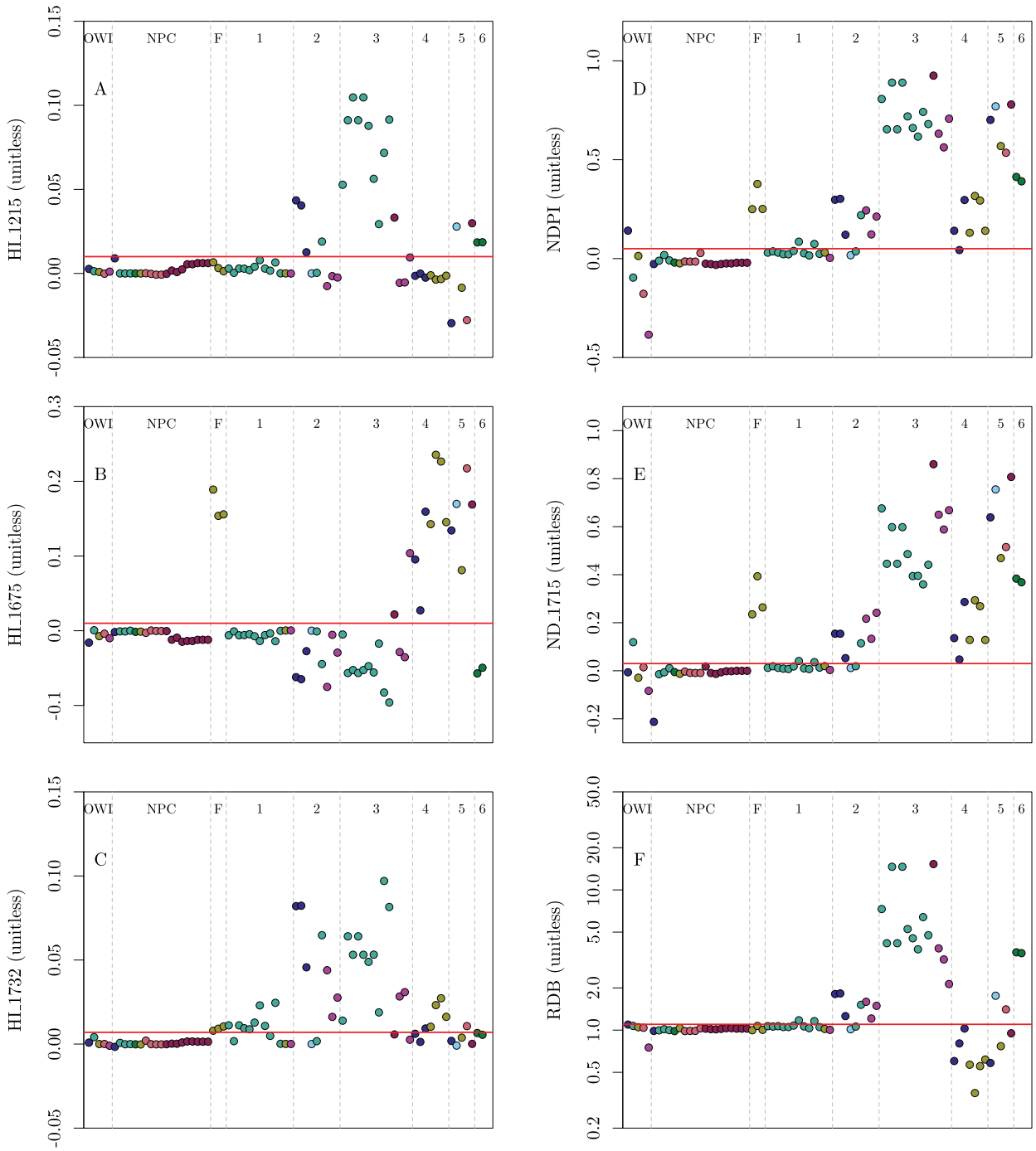

Fig. 6. Evaluation of algorithms using the compiled database. Vertical grey lines separate the groups: Type 1 plastics include clusters 2, 3 and 6; Type 2 plastics include clusters 4 and 5. Cluster 1 has dampened spectral signatures that cannot reliably be targeted, and is composed of plastic samples present in other clusters. Colors follow the colour code per cluster. Red line indicates a threshold used to separate groups. OWI = Organisms, whitecaps, and ice; NPC = non-plastic construction, and F = fiberglass. For further details see Table 3, Figs. 4 and 5. (For interpretation of the references to colour in this figure legend, the reader is referred to the web version of this article.)

and Fig. 12. Photographs and very high spatial resolution imagery of the targets around the Spuikom, with their location in the imagery, are presented in Fig. 11 and Fig. 13 to aid the interpretation of the results. Both terrestrial and floating aquatic targets are evaluated in Figs. 9 and 10 for all three flight lines. Only one flight line (a06c) captured the terrestrial targets in Fig. 12.

The subset of identified targets was consistent with expectations from the application to the compiled dataset. In general, targets identified by HI_1215 and HI_1732 were also identified by RBD (Fig. 9), while those three indexes identified different subsets than those identified by HI_1675 (Fig. 10). The HI_1215 was better at delineating the plastic targets, but the HI_1732 was able to identify more targets, as expected from the compiled dataset analysis. The HI_1732 was the only line height index identifying the PMD bags on grass (Target 01) and the HI_1675 was the only index capable of identifying the small skylights on the club's rooftop (Target 09).

The APGI provided a mixed coverage between HI_1675 and HI_1732 and was the only ratio algorithm to identify the PMD bags on grass

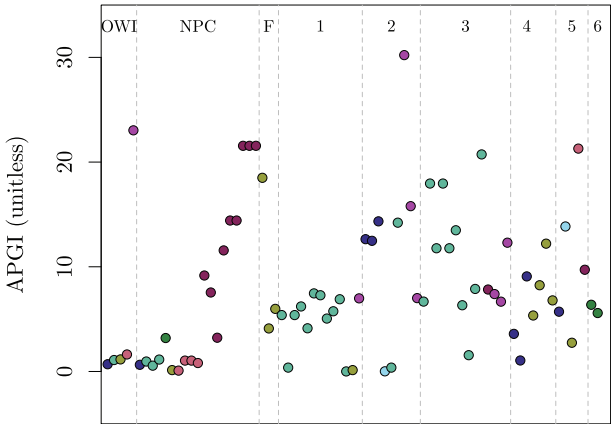

Fig. 7. As Fig. 6 but for the APGI algorithm.

Table 4
Thresholds used for the detection algorithms.

Index	Compiled dataset	Airborne imagery
HI_1215	> 0.010	> 0.007
HI_1675	> 0.010	> 0.010
HI_1732	> 0.007	> 0.013
APGI	–	> 0.500
NDPI	> 0.050	> 0.350
ND_1715	> 0.030	> 0.035
RBD	> 1.100	> 2.330

(Target 01; Fig. 9). The indexes identifying the largest number of targets were the ratio indexes NDPI and the ND_1715, with the latter also providing the most complete delineation of targets for all indexes (Fig. 10). The RBD, while covering similar targets as the HI_1215, showed a higher sensitivity for the detection of Type 1 plastics.

A single threshold was applied to all three flight lines. The thresholds calibrated against pure materials in the compiled dataset could not be directly transferred to the imagery for the majority of the indexes. Table 4 provides a comparison between the thresholds suggested by the analysis with the compiled datasets and those suggested by imagery interpretation. The inconsistency between thresholds used for the compiled dataset and airborne imagery is further discussed in section 4.4.

In addition to the targets in the immediate surrounding of the VZW Inside/Outside club, the flight line a06c also included two commercial centers in Ostend with well identified plastic targets and this additional site was used for evaluation of the algorithms (Figs. 12 and 13). The HI_1732, the RBD, and the NDPI identified all solar panels (Target 13) present over the roof of the Bredene Shopping Center. Typical solar panel construction includes layers of ethylene-vinyl acetate (EVA) copolymer encapsulating the photovoltaic cells (Xu et al., 2018). This is a mixture of plastics from Type 1 (PE and PVC) with the same reflectance spectral shape as other members of this group (Corbari et al., 2020). The solar panels were not identified, however, by the HI_1215 index. The HI_1675 and the APGI indexes were able to identify the larger skylights over the commercial center Bedrijfspark Spuikom (Target 14). The ND_1715 was the only index able to identify both targets.

Table 5 presents a summary of the performance of detection per algorithm, presenting the counts of flight lines in which a given target was identified.

4. Discussion

4.1. Sensor design and performance

Tradeoffs occur between the spectral and spatial resolution of satellite and airborne sensors that influence the ability to detect plastics in the environment. Higher spectral resolution comes at a cost of reducing the signal-to-noise ratio (SNR) of the instrument, as there is less signal reaching the detector when shorter spectral intervals are sampled (Muller-Karger et al., 2018). Reduced SNR is particularly common for aquatic surfaces with very low backscattering and very high water absorption in NIR and SWIR wavelengths (Dekker et al., 2018). In the context of this research, reduced SNR can influence plastic detection in mixed pixels with very small fractional coverage of plastics and when dealing with NIR/SWIR wavelengths where the reflectance signal from the water is very low. The SNR can be improved by increasing the spatial footprint, widening the spectral bands, pointing at a target for more time, or reducing the dynamic range of the detectors (Cetinić et al., 2018).

These tradeoffs can have important consequences for the design of satellite missions to routinely monitor plastics from bright beaches to dark waters. For example, Martínez-Vicente (2022) recently proposed a sensor archetype for plastic litter that would have high spatial resolution (1 to 5 m) to allow shape anomaly detection, include visible and shortwave infrared wavelengths to distinguish plastics within a mixed pixel comprised of different types of debris and to differentiate polymer types. Design considerations for such missions include the detectability of mixed pixels with dilute plastic concentrations (Hueni and Bertschi, 2020), the impact of the underlying substrate on the spectral properties of semi-transparent plastics, and selecting spectral regions in which the atmosphere is not strongly absorbing. This experiment evaluated several of these aspects including mixed pixels of known targets, semi-transparent plastics, differing substrates under the same material, atmospheric influences on the measurement, and sampling from different directions in relation to the sun. In general, the hyperspectral APEX sensor, through different algorithms, was well suited to differentiating between Type 1 and Type 2 plastics on land and emergent plastics on water. Rooftop solar panels (Type 1) and skylights (Type 2), for example, were routinely differentiated in multiple images over the same targets. However, as noted more below, challenges remain in routinely detecting semi-transparent material on grass and floating on water. The spectra of the underlying material can compromise the spectral signature targeted by different algorithms (cf. PMD on grass in Fig. S1 of the supplementary material).

From a mission perspective, the spatial layout of the surface elements, the spatial resolution of the acquisition and the layout of the observation grid will define the magnitude of contrast reduction due to mixed pixels. In this study, we used unprojected imagery at a nominal spatial resolution of 1.6 m. This resolution is compatible with the scale of observation of WorldView-3 (NDPI, RBD), but it is one order of magnitude higher than that of MSI/Sentinel-2 (APGI). Airborne sensors such as APEX, AVIRIS, and PRISM do not have a consistent spatial resolution between acquisition due to changes in aircraft height and turbulence effects that disturb the smooth scanning of the surface. The application of the same algorithms to different flight lines in Figs. 9 and 10 provides an example of these spatial effects, with features better delineated or identified in one flight line over the others, depending on the algorithm.

4.2. Algorithm design and performance

A primary aim of any remote sensing algorithm is to maximize detection, possibly over different sensor types and environmental conditions, and to minimize false positives. Some plastic samples presented highly dampened optical signatures to be exploited for detection (cf. Cluster 1 in Fig. 5). While this could be an artefact of how the samples were measured (e.g., thin layers of material), it can represent real plastic material in the environment. Therefore, even with optimal data (controlled experiments with the pure plastic material filling the field of view of the sensor) optical information in the NIR to SWIR range cannot detect all plastic samples, resulting in false negatives.

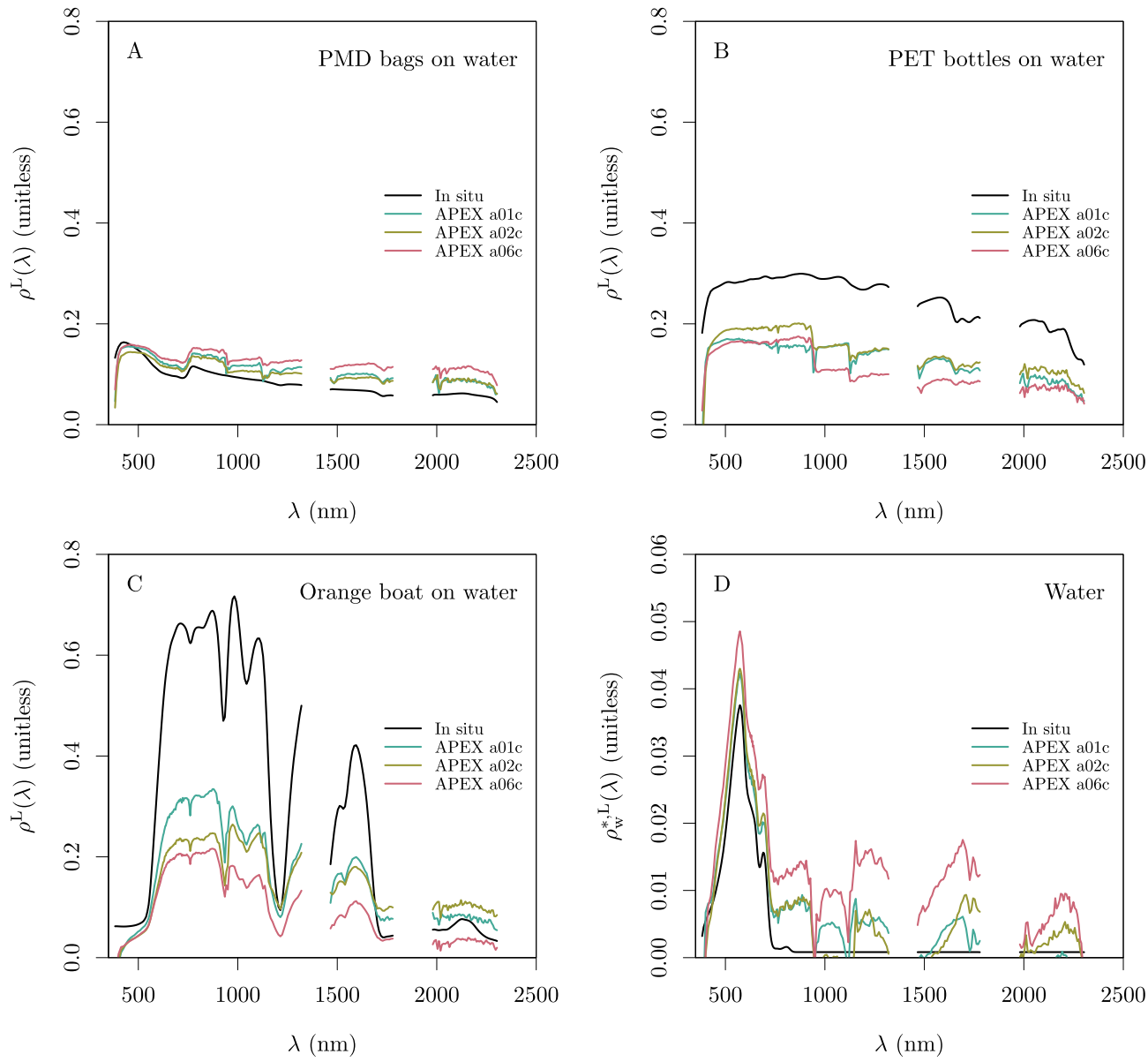

Fig. 8. Example comparison between the in situ ASD and APEX reflectance for the different flight lines. Subplots A, B and C show three validation targets on water. Subplot D shows the water, used as a calibration point. Note the near-zero and negative values of the station average water reflectance from APEX.

In general, the algorithms performed as expected from the compiled database analysis and provided consistent results among each other and among flight lines. Ratio algorithms with high sensitivity (NDPI or ND_1715) specific to plastic but insensitive to plastic type can be used to map the presence of plastics. The line height algorithm HI_1675 can be used for the identification of Type 2 plastics, and HI_1732 can be used for the identification of Type 1 plastics. The HI_1732 showed better performance than the HI_1215, which was not capable of identifying the large skylights (Target 13). The RBD is expected to identify plastics from Types 1 and 3, and therefore can be used by difference to the HI_1732 to identify plastics from Type 3.

The APGI was not suitable for plastic detection in the compiled dataset due to positive detections for wood and ice. However, the index can still find applications in sceneries where ice and wood are not present. For example, ice was not present in the Spuikom during the measurements and it is possible that wood targets were also not present on land, since the APGI did not identified targets not identified by other indexes. However, due to the potential false positive with wood, other indices may be preferred.

The line height indexes centered at 1215, 1675 and 1732 nm were more sensitive to mixed pixels and identified the central pixels of each target. Lowering the threshold of those indexes expanded the identification of peripherial pixels of the targets but also added false positives to the imagery. The HI_1675 was designed to capture the spectral signature unique to Type 2 plastics, with a strong absorption band around 1660 nm, but includes a compromise in the choice of wavebands such as to also capture the signal of fiberglass. As presented in section 3.1, fiberglass is a glass fiber reinforced plastic and presents the same spectral shape as PET between 1500 and 1800 nm, though the main absorption bands is shifted to 1684 nm. The proposed HI_1675 index showed sensitivity to detect Type 2 plastics in the imagery, including the thin stripes of semi-transparent roof sheets (Target 09, small skylights). The algorithm identified the whole area of the rooftop containing the skylights likely due to the narrowness of the skylights and mixed pixel effects.

The generalist broadband algorithm developed here, ND_1715, is optimized for a part of the SWIR spectrum that appears to be unique to plastics – from 1550 to 1750 nm. In this wavelength range, plastic

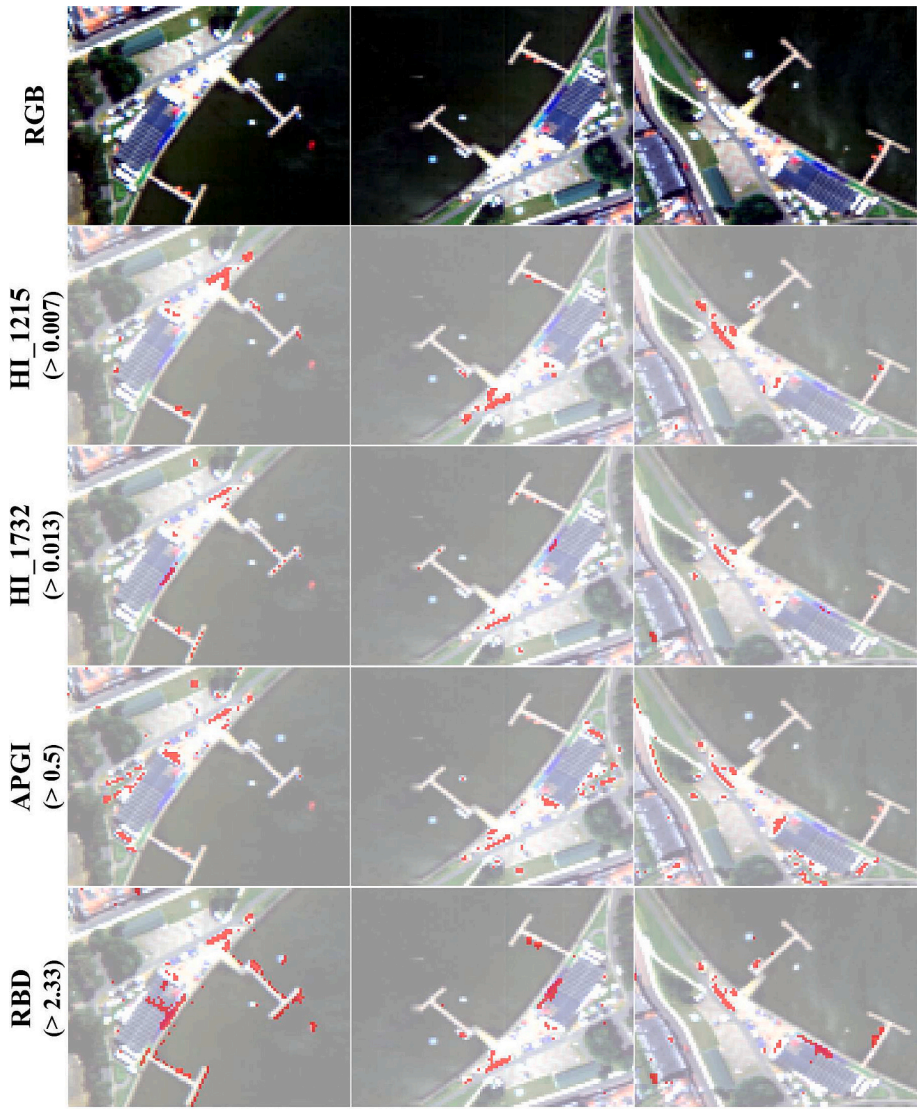

Fig. 9. Pseudo true colour Red-Green-Blue (RGB) and transparent RGB background overlaid with the red mask of the Hydrocarbon Index at 1215 and 1732 nm (HI_1215 and HI_1732), Advanced Plastic Greenhouse Index (APGI), and Relative Band Depth (RBD) end-products derived from the APEX hyperspectral images obtained on 27 June 2019 over the Spuikom, Belgium. Values in parenthesis indicate the threshold used to create the red masks. (For interpretation of the references to colour in this figure legend, the reader is referred to the web version of this article.)

reflectance from the field experiment and historic database present a decreasing spectral slope. This is consistent with the 1725 nm spectral absorption band ubiquitous to floating microplastics from the major ocean gyres (Garaba and Dierssen, 2018), as well as a host of other macroplastics LDPE and HDPE macroplastics, like the white, orange, and blue boats targeted here and the EVA coating on the solar panels. This algorithm leverages the general decrease in reflectance from 1600 to 1735 nm evident across nearly all of the plastic types with a normalized difference of two bands centered at 1610 nm (1590 to 1630 nm) and 1710 nm (1695 to 1735 nm).

Plastic targets floating on water were only partially identified or missed by most algorithms and flight lines. Considering the relatively small target size and imagery resolution, it is expected that the mixed signal with the darker water background reduced the magnitude of the features targeted by each algorithm. The boats (Target 04 and 06), however, were more easily identified by the different algorithms. Considering that their size is even smaller than the floating PMD bags and PET bottles targets, it is likely that another important aspect is the thickness of the plastic layer. The PMD bags form two thin sheets and result in a semi-transparent layer that mixes the signal from the underlying material. This can be seen for the in situ data in Fig. S1 of the supplementary material. The body of the PET bottles is transparent in the visible range and potentially semi-transparent in the SWIR at the thickness of the material, which is also supported by the in situ data in Fig. S1. Therefore the detection of thin floating plastic objects, even if large, is prone to false negatives.

4.3. *The impact of atmospheric correction errors*

The impact of biases in atmospheric correction also needs to be considered for algorithm design and evaluation. This can be critical on spectral ranges where surfaces in the imagery are dark in comparison with the atmosphere. One such example is the observation of floating materials on water using SWIR wavebands as necessary for plastic discrimination.

In this study we have used the ELM to perform atmospheric correction, as we had in situ data to control the atmospheric correction results, rather than just quantify the performance of a given physically based method. In fact, the ELM can enforce that the observations of different sensors match (in a regression sense). The ELM is a valid approach for

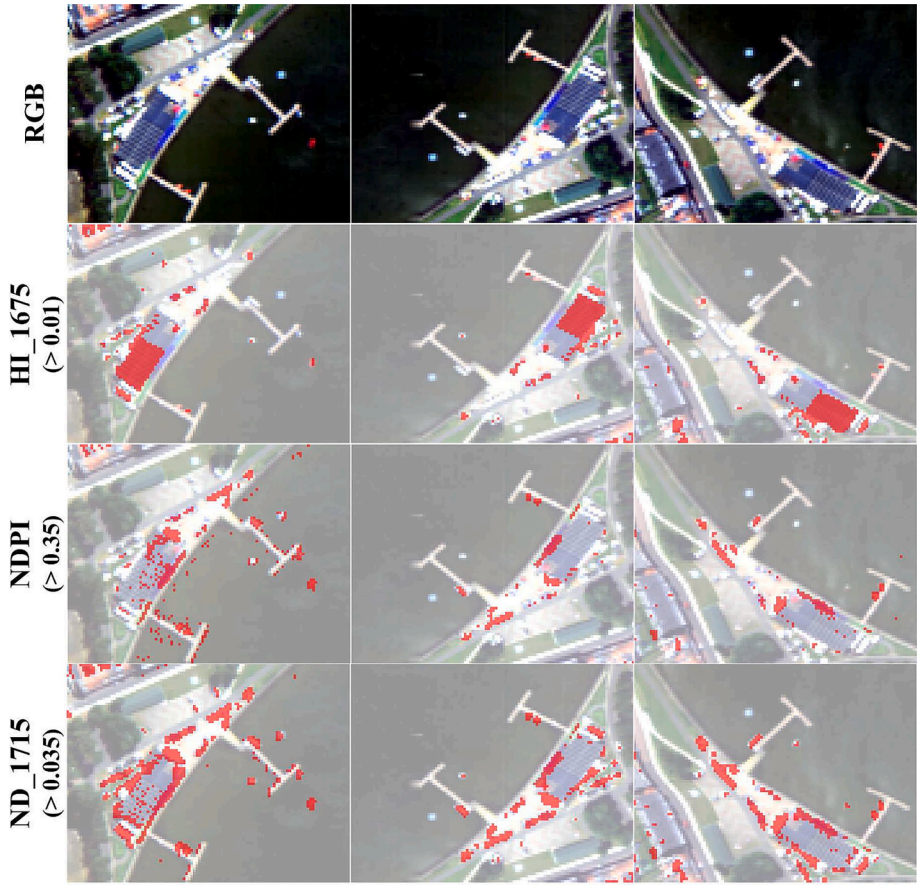

Fig. 10. As in Fig. 9, but showing the pseudo true colour Red-Green-Blue (RGB) and transparent RGB background overlaid with the red mask of the Hydrocarbon Index at 1675 nm (HI_1675), Normalized Difference Plastic Index (NDPI), and Normalized Difference at 1610 and 1715 nm (ND_1715) end-products derived from the APEX hyperspectral images obtained on 27 June 2019 over the Spuikom, Belgium. Values in parenthesis indicate the threshold used to create the red masks. (For interpretation of the references to colour in this figure legend, the reader is referred to the web version of this article.)

the condition evaluated in this study: (1) small spatial extent to assume constant atmospheric properties over the scene; (2) small time interval between in situ and imagery compared to the scale of change in the illumination and reflection properties of the targets; and (3) calibration targets represent pure (not mixed) signal in the sensor data. Nonetheless, biases are expected in the darker end of the reflectance range, as the contributions of those data points for the cost function of the regression are smaller. Hence, the reflectance retrieval over water pixels of the Spuikom lagoon had high relative error.

All line height indexes were robust to atmospheric correction errors that caused the water reflectance to be near zero or negative (Section 3.4). This bias over water was higher for flight lines a01c and a02c compared to a06c. The application of the ratio algorithms to processed imagery without an initial "low reflectance" mask would result in high number of false positives over water (cf. Fig. S9 in the supplementary material). This masking, however, was arbitrary and can be expected to depend on the scenery and type and magnitude of the AC bias. Interestingly, while the NDPI and the ND_1715 had similar performances with the compiled dataset, the proposed ND_1715 algorithm was more robust to atmospheric correction errors and allowed for a consistent threshold between compiled dataset and imagery. It is possible that the use of a second set of band differences at wavelengths longer than 2000 nm is the cause for the higher sensitivity of the NDPI to atmospheric correction errors, as a similar sensitivity was observed for the RBD which also uses a waveband longer than 2000 nm.

It is worth noting that while the line height algorithms showed less contrast than the ratio algorithms, they were more robust to atmospheric correction errors. Therefore the different sensitivities to atmospheric correction and contrast reduction due to spatial averaging for line-heights and ratio indexes suggest a potential complementarity. Such complementarity is further supported by the specificity of some indexes to specific plastic groups.

4.4. Algorithm detection thresholds

Thresholds such as the ones applied directly to the individual indexes used here are a unidimensional decision tree model, manually (qualitative) or statistically (quantitative) optimized to maximize the classification of the desired target while minimizing false positives. Ideally, thresholds would be calibrated against a set of known materials and applied directly to arbitrary imagery. Results presented in Table 4 however show that this was not the case for most algorithms. Considering the analysis in Fig. 6, it could be expected that spatial averaging would require threshold values to be reduced for application to imagery for indexes with lower contrast. However, only HI_1215 had an imagery threshold lower than the calibration threshold. This suggests the difference is dominated by spectrally featured atmospheric correction errors. Moreover, the difference in threshold values was larger for ratio indexes than for line-height indexes (cf. Section S3 of the supplementary material). The empirical line method used here for atmospheric correction provides an independent regression line per waveband, potentially resulting in higher interband variation than physically based methods that impose a spectral structure to atmospheric attenuation.

Interestingly, the calibrated thresholds for the two algorithms proposed in this study, HI_1675 and ND_1715 were on only ones that could be directly transferred to the imagery. It is possible that for the ND_1715,

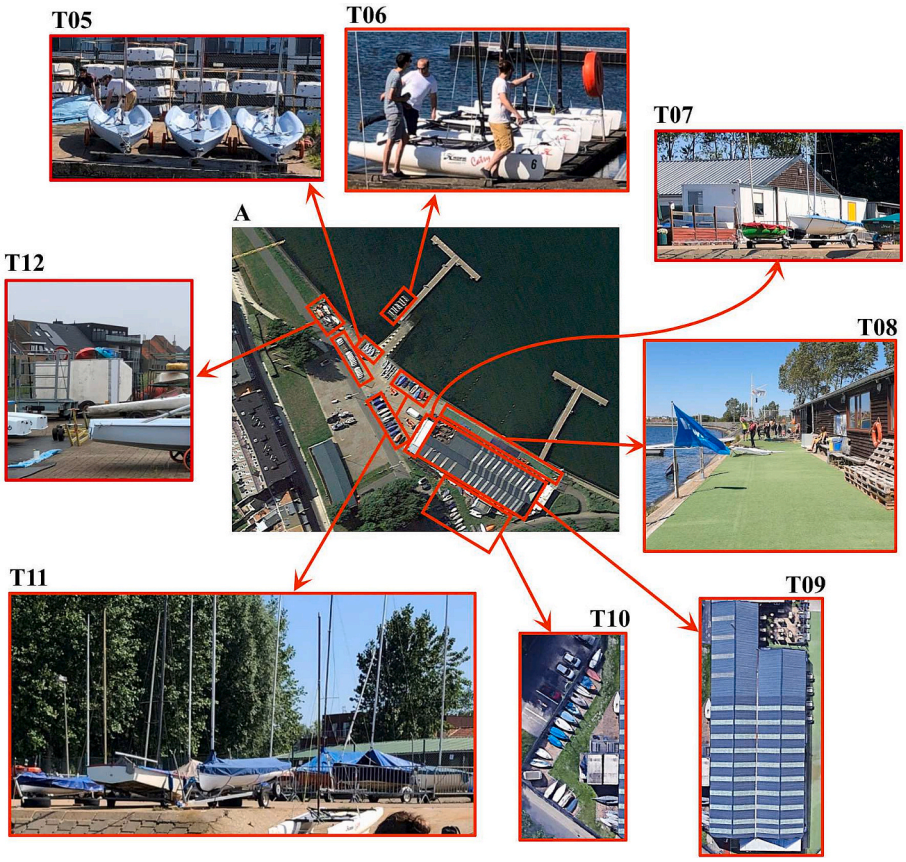

Fig. 11. Plastic objects and structures ("Targets", T) in the VZW Inside/Outside club, Ostend. (A) Google Earth imagery for August/2019, rotated to the orientation of the observation grid of flight line a06c; (T05) Stacked blue and white boats on shore; (T06) Hobie catamaran sailboats; (T07) Portable cabin (Pullman, Portakabin) coated in PE; (T08) Artificial grass (typically made of PE, PP and PA); (T09) Rooftop with skylight strips (likelly PMMA or PC); (T10) and (T11) parked boats covered by white and blue tarps (likelly PMMA); (T12) Additional cabin and boats. Objects identified from pictures and satelite imagery. (For interpretation of the references to colour in this figure legend, the reader is referred to the web version of this article.)

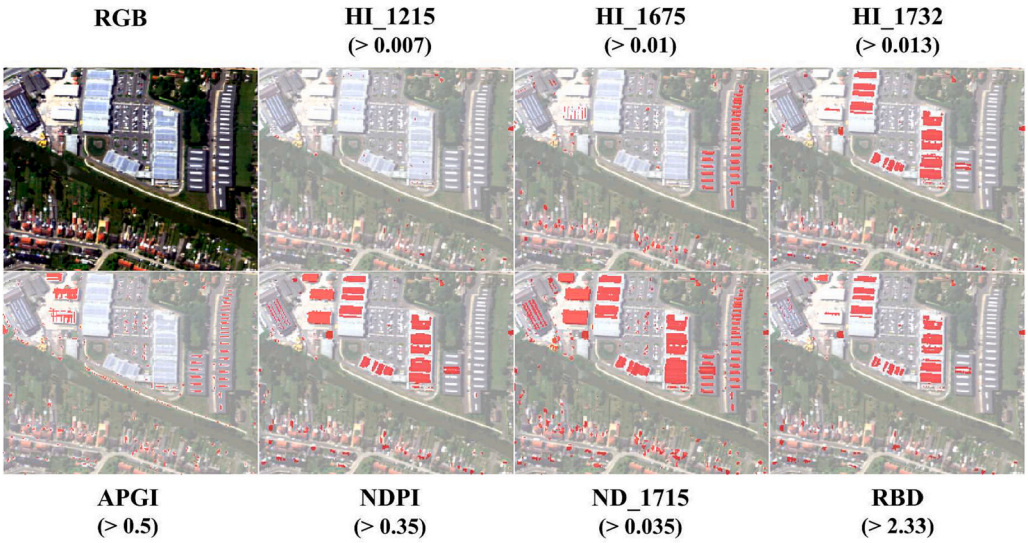

Fig. 12. Pseudo true colour image overlaid with the red mask of the Hydrocarbon Indexes at 1215, 1675 and 1732 nm (HI_1215, HI_1675, HI_1732), the Advanced Plastic Greenhouse Index (APGI), the Normalized Difference Plastic Index (NDPI), the Normalized Difference at 1610 and 1715 nm (NDI_1715), and the Relative Band Depth (RBD) index applied to APEX hyperspectral image flight line a06c obtained on 27 June 2019 over the Bredene Shopping Center area, Belgium. (For interpretation of the references to colour in this figure legend, the reader is referred to the web version of this article.)

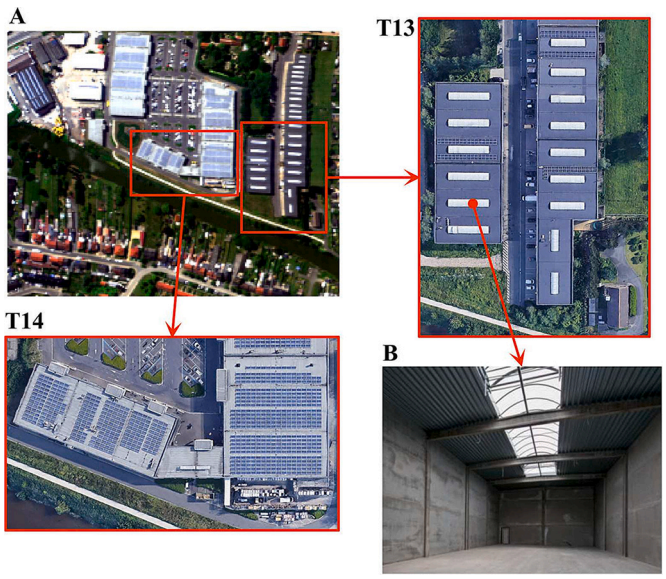

Fig. 13. Identification of plastic targets on rooftops surrounding the Spuikom. (A) Pseudo true colour composite of a spatial subset of flight line a06c; (T13) Google Earth imagery showing the skylights on the roof of the Business park Spuikom; (T14) Google Earth imagery showing solar pannels on the roof of the Bredene Shopping Center; (B) Picture from the inside of a building in the Business park Spuikom confirming the presence of skylights. Picture retrieved from the website of the company managing the Business park Spuikom, https://www.globalestategroup.eu/.

the inclusion of only two wavebands covering a relatively narrow range of wavelengths when compared to the other ratio indexes, makes it more robust to atmospheric correction errors. However, the reason for the relative robustness of HI_1675 when compared with other indexes is unclear. More studies are necessary to establish a general recommendation in terms of threshold values to be applied operationally.

It is worth noting that the thresholds provided in this study are specific to the reflectance quantity used. While the conversion from hemispherical-directional to Lambert-equivalent bi-hemispherical reflectance involves a constant scaling factor (π sr^{-1}), the algorithms contain addition or subtraction operations before the normalization, and the scaling factor does not cancel out.

5. Conclusions

The analysis of normalized spectra in the NIR-SWIR shows that plastics appear to have unique spectral signatures when considering other common surface materials. Several available algorithms are able to capture this signature for plastic detection under ideal laboratory conditions, namely in the absence of mixed signal from surrounding or overlaid materials. Laboratory and field data support that mixed signals are the main challenge for plastic detection by remote sensing. Some plastic materials are common as thin films, and may not present sufficient optical depth to be detected, unless aggregated into multiple layers. Similarly, the size of the material and aggregation may not be large enough to completely fill the field of view of the detector element, resulting in mixed signals from surrounding surfaces even at high plastic optical depths. The development of sensitive algorithms that enhance contrast between plastic and non-plastic can remediate these effects to some extent, and most algorithms evaluated in this research showed a high degree of specificity and sensitivity to at least one plastic type.

Therefore, except for optically thin films, plastic detection from remote platforms appears feasible with current sensors and algorithms when plastic structures cover the full pixel footprint. The full coverage also prevents reduction of the signal magnitude when plastic materials are present over dark backgrounds such as water. Detection of subpixel plastic surfaces is highly uncertain, depending on brightness contrast and fractional coverage. Here we showed that relatively broad band indexes were sufficient for plastic detection, therefore allowing sensor design for plastic detection with limited broader bands, but comparatively higher spatial resolution and SNR. For plastic type detection, finer spectral resolution is necessary, which can compromise spatial resolution and SNR. In this context, sensors with several relatively narrow bands in the SWIR might represent a flexible alternative, allowing for waveband aggregation to increase SNR for the detection of plastics, and more fine spectral resolution for identification of plastic types, at lower SNR, on the identified plastic structures. At least three different plastic types, based on unique spectral signatures in the NIR-SWIR, seem feasible to be differentiated by remote sensing based on optical signatures.

Funding

AC was funded by the BELSPO Stereo III project HYPERMAQ (SR/00/335). HMD was funded by the Belgian/U.S. Fulbright Scholars Program and NASA Ocean Biology and Biogeochemistry project Advancing Remote Sensing of Microplastics (#80NSSC21K0515). LID, GE, EK and

Table 5
Detection of plastic target from the APEX imagery, considering the thresholds presented in Table 4. Counts represent the number of flight lines in which each target was identified with a given algorithm and threshold. The alphanumeric code preceding each entry corresponds to the target numbers following Fig. 1, Fig. 11 and Fig. 13.

Target	Plastic type	HI Indices			Ratio Indices			
		1215	1675	1732	APGI	NDPI	ND_1715	RDB
Terrestrial								
T01 - PMD bags on grass	1	–	–	3	3	–	–	–
T05 - Blue and white boats	1	3	–	3	3	3	3	3
T07 - White trailer	1	2	–	–	3	3	3	1
T08 - Synthetic grass	1	–	–	1	–	3	3	3
T09 - Skylights on boathouse	2	–	3	–	–	1	1	–
T10 - Tarp-covered boats 1	2	–	3	–	3	–	3	–
T11 - Tarp-covered boats 2	2	–	3	–	–	1	3	–
T12 - Kayaks and trailer	1,2	3	3	–	3	3	3	2
T13 - Skylights on shops[†]	2	–	1	–	1	–	1	–
T14 - Solar panels on shops[†]	1	–	–	1	–	1	1	1
Aquatic								
T02 - PMD bags on water	1	–	–	–	–	1	1	–
T03 - PET bottles on water	1,2	–	2	–	1	1	3	–
T04 - Orange boats	1	3	3	2	–	3	3	3
T06 - White hobicats	1	3	–	–	–	3	3	3

[†] Target only imaged in one flight line (a06c).

SS were supported by the Flanders Innovation & Entrepreneurship (VLAIO) in the capacity of the PLUXIN project 'Plastic Flux for Innovation and Business Opportunities in Flanders' (cSBO, Project Number HBC.2019.2904).

CRediT authorship contribution statement

Alexandre Castagna: Formal analysis, Investigation, Methodology, Visualization, Writing – original draft, Writing – review & editing. **Heidi M. Dierssen:** Conceptualization, Investigation, Methodology, Resources, Supervision, Writing – original draft, Writing – review & editing. **Lisa I. Devriese:** Investigation, Resources, Project administration, Writing – review & editing. **Gert Everaert:** Investigation, Resources, Writing – review & editing. **Els Knaeps:** Conceptualization, Resources, Project administration, Writing – review & editing. **Sindy Sterckx:** Conceptualization, Resources, Project administration, Writing – review & editing.

Declaration of Competing Interest

The authors declare no conflicts of interest.

Data availability

Hyperspectral measurements of the artificial targets are available on PANGAEA (https://doi.org/10.1594/PANGAEA.937185). All other data used in this study is available from the authors on reasonable request.

Acknowledgments

The authors would also like to thank colleagues for their contribution in the preparation and execution of these tests: Shungudzemwoyo P. Garaba, Mattias Bossaer, Alexander Hooyberg, Jonas Lescroart, Johan Mijnendonckx, Stan Pannier and Matthias Sandra. Shungudzemwoyo P. Garaba kindly provided the spectral reflectance compilation of plastics and construction materials and performed the interdetector step correction in the in situ data. Permission (number 219119/CVH 16-EH-U-19-1923) from Coastal Division of the Maritime Services and Coastal Agency (government of Flanders) for the placement of a plastic construction in the Spuikom. The authors thank the surf club VVW Inside – Outside, the Maritime Services and Coastal Agency (government of Flanders), the Blue Cluster, and the province of West-Flanders for their support. The authors appreciate the suggestions provided by two anonymous reviewers, that considerably contributed to improve the final manuscript.

Appendix A. Supplementary data

Supplementary data to this article can be found online at https://doi.org/10.1016/j.rse.2023.113834.

References

Asadzadeh, S., de Souza Filho, C.R., 2016. Investigating the capability of worldview-3 superspectral data for direct hydrocarbon detection. Remote Sens. Environ. 173, 162–173.

Bivand, R., Keitt, T., Rowlingson, B., 2021. rgdal: Bindings for the 'geospatial' data abstraction library. https://CRAN.R-project.org/package=rgdal r package version 1.5-23.

Castagna, A., Amadei Martínez, L., Bogorad, M., Daveloose, I., Dasseville, R., Dierssen, H. M., Beck, M., Mortelmans, J., Lavigne, H., Dogliotti, A., Doxaran, D., Ruddick, K., Vyverman, W., Sabbe, K., 2022. Optical and biogeochemical properties of diverse Belgian inland and coastal waters. Earth Syst. Sci. Data 14 (6), 2697–2719.

Castagna, A., Johnson, B.C., Voss, K., Dierssen, H.M., Patrick, H., Germer, T.A., Sabbe, K., Vyverman, W., Jun 2019. Uncertainty in global downwelling plane irradiance estimates from sintered polytetrafluoroethylene plaque radiance measurements. Appl. Opt. 58 (16), 4497–4511.

Cetinić, I., McClain, C.R., Werdell, P.J., 2018. Ocean Color Instrument (oci) Concept Design Studies, Volume 7. NASA Goddard Space Flight Center, Greenbelt, Maryland, pACE. Tech. rep.,Technical Report Series.

Corbari, L., Maltese, A., Capodici, F., Mangano, M.C., Sarà, G., Ciraolo, G., 2020. Indoor spectroradiometric characterization of plastic litters commonly polluting the mediterranean sea: toward the application of multispectral imagery. Sci. Rep. 10 (1), 19850.

Dekker, A.G., Pinnel, N., Gege, P., Briottet, X., Court, A., Peters, S.W., Turpie, K., Sterckx, S., Costa, M., Giardino, C., Brando, V., Braga, F.Bergeron, Heege, T., Pflug, B., 2018. Feasibility study for an aquatic ecosystem earth observing system. CEOS. Tech. rep.

Dierssen, H.M., 2019. Hyperspectral measurements, parameterizations, and atmospheric correction of whitecaps and foam from visible to shortwave infrared for ocean color remote sensing. Frontiers. Earth Sci. 7.

Forgy, E.W., 1965. Cluster analysis of multivariate data : efficiency versus interpretability of classifications. Biometrics 21, 768–769.

Freitas, S., Silva, H., Silva, E., 2021. Remote hyperspectral imaging acquisition and characterization for marine litter detection. Remote Sens. 13 (13).

Garaba, S.P., Arias, M., Corradi, P., Harmel, T., de Vries, R., Lebreton, L., 2021. Concentration, anisotropic and apparent colour effects on optical reflectance properties of virgin and ocean-harvested plastics. J. Hazard. Mater. 406, 124290.

Garaba, S.P., Castagna, A., Devriese, L.I., Dierssen, H.M., Everaert, G., Knaeps, E., Sterckx, S., 2021. Spectral reflectance measurements of dry and wet plastic materials, asphalt, concrete klinker from UV-350 nm to SWIR-2500 nm around Spuikom, Belgium.

Garaba, S.P., Dierssen, H.M., 2017. Spectral reference library of 11 types of virgin plastic pellets common in marine plastic debris.

Garaba, S.P., Dierssen, H.M., 2018. An airborne remote sensing case study of synthetic hydrocarbon detection using short wave infrared absorption features identified from marine-harvested macro- and microplastics. Remote Sens. Environ. 205, 224–235.

Garaba, S.P., Dierssen, H.M., 2020. Hyperspectral ultraviolet to shortwave infrared characteristics of marine-harvested, washed-ashore and virgin plastics. Earth Syst. Sci. Data 12 (1), 77–86.

Goddijn-Murphy, L., Dufaur, J., 2018. Proof of concept for a model of light reflectance of plastics floating on natural waters. Mar. Pollut. Bull. 135, 1145–1157.

Guo, X., Li, P., 2020. Mapping plastic materials in an urban area: development of the normalized difference plastic index using worldview-3 superspectral data. ISPRS J. Photogramm. Remote Sens. 169, 214–226.

Hijmans, R.J., 2021. raster: Geographic data analysis and modeling. https://CRAN.R-project.org/package=raster r package version 3.4-13.

Hu, C., 2021. Remote detection of marine debris using satellite observations in the visible and near infrared spectral range: challenges and potentials. Remote Sens. Environ. 259, 112414.

Hu, L., Hu, C., Ming-Xia, H., 2017. Remote estimation of biomass of ulva prolifera macroalgae in the yellow sea. Remote Sens. Environ. 192, 217–227.

Hueni, A., Bertschi, S., 2020. Detection of sub-pixel plastic abundance on water surfaces using airborne imaging spectroscopy. In: IGARSS 2020 - 2020 IEEE International Geoscience and Remote Sensing Symposium, pp. 6325–6328.

Hueni, A., Bialek, A., 2017. Cause, effect, and correction of field spectroradiometer interchannel radiometric steps. IEEE J. Sel.Top. Appl. Earth Obs. Remote Sens. 10 (4), 1542–1551.

Jehle, M., Hueni, A., Lenhard, K., Baumgartner, A., Schaepman, M.E., 2015. Detection and correction of radiance variations during spectral calibration in apex. IEEE Geosci. Remote Sens. Lett. 12 (5), 1023–1027.

Khan, A.L., Dierssen, H., Schwarz, J.P., Schmitt, C., Chlus, A., Hermanson, M., Painter, T. H., McKnight, D.M., 2017. Impacts of coal dust from an active mine on the spectral reflectance of arctic surface snow in svalbard, Norway. J. Geophys. Res. Atmos. 122 (3), 1767–1778.

Kühn, F., Oppermann, K., Hörig, B., 2004. Hydrocarbon index – an algorithm for hyperspectral detection of hydrocarbons. Int. J. Remote Sens. 25 (12), 2467–2473.

Knaeps, E., Sterckx, S., Strackx, G., Mijnendonckx, J., Moshtaghi, M., Garaba, S.P., Meire, D., 2021. Hyperspectral-reflectance dataset of dry, wet and submerged marine litter. Earth Syst. Sci. Data 13 (2), 713–730.

Knaeps, E., Strackx, G., Meire, D., Sterckx, S., Mijnendonckx, J., Moshtaghi, M., 2020. Hyperspectral reflectance of marine plastics in the vis to swir.

Kokaly, R.F., Clark, R.N., Swayze, G.A., Livo, K.E., Hoefen, T.M., Pearson, N.C., Wise, R. A., Benzel, W., Lowers, H.A., Driscoll, R.L., Klein, A.J., 2017. Usgs spectral library version 7. U.S. Geological Survey, Reston, VA. Tech. rep.

Lavender, S., 2022. Detection of waste plastics in the environment: application of copernicus earth observation data. Remote Sens. 14 (19).

Lee, Z., Wei, J., Shang, Z., Garcia, R., Dierssen, H., Ishizaka, J., Castagna, A., 2019. On-water radiometry measurements: Skylight-blocked approach and data processing. Tech. rep. In: Zibordi, G., Voss, K.J., Johnson, B.C., Mueller, J.L. (Eds.), Protocols for Satellite Ocean Colour Data Validation: In Situ Optical Radiometry. IOCCG.

Martínez-Vicente, V., 2022. The need for a dedicated marine plastic litter satellite mission. Nat. Rev. Earth Environ. 3 (11), 728–729.

Martínez-Vicente, V., Clark, J.R., Corradi, P., Aliani, S., Arias, M., Bochow, M., Bonnery, G., Cole, M., Cózar, A., Donnelly, R., Echevarría, F., Galgani, F., Garaba, S. P., Goddijn-Murphy, L., Lebreton, L., Leslie, H.A., Lindeque, P.K., Maximenko, N., Martin-Lauzer, F.-R., Moller, D., Murphy, P., Palombi, L., Raimondi, V., Reisser, J., Romero, L., Simis, S.G., Sterckx, S., Thompson, R.C., Topouzelis, K.N., van Sebille, E., Veiga, J.M., Vethaak, A.D., 2019. Measuring marine plastic debris from space: initial assessment of observation requirements. Remote Sens. 11 (20).

Maximenko, N., Corradi, P., Law, K.L., Van Sebille, E., Garaba, S.P., Lampitt, R.S., Galgani, F., Martinez-Vicente, V., Goddijn-Murphy, L., Veiga, J.M., Thompson, R.C., Maes, C., Moller, D., Löscher, C.R., Addamo, A.M., Lamson, M.R., Centurioni, L.R., Posth, N.R., Lumpkin, R., Vinci, M., Martins, A.M., Pieper, C.D., Isobe, A., Hanke, G., Edwards, M., Chubarenko, I.P., Rodriguez, E., Aliani, S., Arias, M., Asner, G.P., Brosich, A., Carlton, J.T., Chao, Y., Cook, A.-M., Cundy, A.B., Galloway, T.S.,

Giorgetti, A., Goni, G.J., Guichoux, Y., Haram, L.E., Hardesty, B.D., Holdsworth, N., Lebreton, L., Leslie, H.A., Macadam-Somer, I., Mace, T., Manuel, M., Marsh, R., Martinez, E., Mayor, D.J., Le Moigne, M., Molina Jack, M.E., Mowlem, M.C., Obbard, R.W., Pabortsava, K., Robberson, B., Rotaru, A.-E., Ruiz, G.M., Spedicato, M. T., Thiel, M., Turra, A., Wilcox, C., 2019. Toward the integrated marine debris observing system. Front. Marine Sci. 6.

Mobley, C.D., 1994. Light and water: Radiative transfer in natural waters. Academic Press, San Diego, CA.

Muller-Karger, F.E., Hestir, E., Ade, C., Turpie, K., Roberts, D.A., Siegel, D., Miller, R.J., Humm, D., Izenberg, N., Keller, M., Morgan, F., Frouin, R., Dekker, A.G., Gardner, R., Goodman, J., Schaeffer, B., Franz, B.A., Pahlevan, N., Mannino, A.G., Concha, J.A., Ackleson, S.G., Cavanaugh, K.C., Romanou, A., Tzortziou, M., Boss, E.S., Pavlick, R., Freeman, A., Rousseaux, C.S., Dunne, J., Long, M.C., Klein, E., McKinley, G.A., Goes, J., Letelier, R., Kavanaugh, M., Roffer, M., Bracher, A., Arrigo, K.R., Dierssen, H., Zhang, X., Davis, F.W., Best, B., Guralnick, R., Moisan, J., Sosik, H.M., Kudela, R., Mouw, C.B., Barnard, A.H., Palacios, S., Roesler, C., Drakou, E.G., Appeltans, W., Jetz, W., 2018. Satellite sensor requirements for monitoring essential biodiversity variables of coastal ecosystems. Ecol. Appl. 28 (3), 749–760.

Qi, L., Yao, Y., English, D.E., Ma, R., Luft, J., Hu, C., 2021. Remote sensing of brine shrimp cysts in salt lakes. Remote Sens. Environ. 266, 112695.

Team, R.Core, 2020. R: A language and environment for statistical computing. Foundation for Statistical Computing, Vienna, Austria ersion 3.6.3. https://www.r-project.org/index.html.

Schaepman, M.E., Jehle, M., Hueni, A., D'Odorico, P., Damm, A., Weyermann, J., Schneider, F.D., Laurent, V., Popp, C., Seidel, F.C., Lenhard, K., Gege, P., Küchler, C., Brazile, J., Kohler, P., De Vos, L., Meuleman, K., Meynart, R., Schläpfer, D., Kneubühler, M., Itten, K.I., 2015. Advanced radiometry measurements and earth science applications with the airborne prism experiment (apex). Remote Sens. Environ. 158, 207–219.

Smith, G.M., Milton, E.J., 1999. The use of the empirical line method to calibrate remotely sensed data to reflectance. Int. J. Remote Sens. 20 (13), 2653–2662.

Tanaka, A., Sasaki, H., Ishizaka, J., Apr 2006. Alternative measuring method for water-leaving radiance using a radiance sensor with a domed cover. Opt. Express 14 (8), 3099–3105.

Taubert, D.R., Hollandt, J., Sperfeld, P., Pape, S., Höpe, A., Hauer, K.-O., Gege, P., Schwarzmaier, T., Lenhard, K., Baumgartner, A., 2013. Providing radiometric traceability for the calibration home base of DLR by PTB. AIP Conf. Proc. 1531 (1), 376–379.

van Sebille, E., Aliani, S., Law, K.L., Maximenko, N., Alsina, J.M., Bagaev, A., Bergmann, M., Chapron, B., Chubarenko, I., Cózar, A., Delandmeter, P., Egger, M., Fox-Kemper, B., Garaba, S.P., Goddijn-Murphy, L., Hardesty, B.D., Hoffman, M.J., Isobe, A., Jongedijk, C.E., Kaandorp, M.L.A., Khatmullina, L., Koelmans, A.A., Kukulka, T., Laufkötter, C., Lebreton, L., Lobelle, D., Maes, C., Martinez-Vicente, V., Maqueda, M.A.M., Poulain-Zarcos, M., Rodríguez, E., Ryan, P.G., Shanks, A.L., Shim, W.J., Suaria, G., Thiel, M., van den Bremer, T.S., Wichmann, D., Feb 2020. The physical oceanography of the transport of floating marine debris. Environ. Res. Lett. 15 (2), 023003.

Wang, M., Hu, C., Cannizzaro, J., English, D., Han, X., Naar, D., Lapointe, B., Brewton, R., Hernandez, F., 2018. Remote sensing of sargassum biomass, nutrients, and pigments. Geophys. Res. Lett. 45 (22), 12359–12367.

Xu, Y., Li, J., Tan, Q., Peters, A.L., Yang, C., 2018. Global status of recycling waste solar panels: a review. Waste Manag. 75, 450–458.

Zhang, P., Du, P., Guo, S., Zhang, W., Tang, P., Chen, J., Zheng, H., 2022. A novel index for robust and large-scale mapping of plastic greenhouse from sentinel-2 images. Remote Sens. Environ. 276, 113042.